Science Advances
AAAS

advances.sciencemag.org/cgi/content/full/6/11/eaaz0510/DC1

Supplementary Materials for

Computationally aided, entropy-driven synthesis of highly efficient and durable multi-elemental alloy catalysts

Yonggang Yao, Zhenyu Liu, Pengfei Xie, Zhennan Huang, Tangyuan Li, David Morris, Zou Finfrock, Jihan Zhou, Miaolun Jiao, Jinlong Gao, Yimin Mao, Jianwei Miao, Peng Zhang, Reza Shahbazian-Yassar*, Chao Wang*, Guofeng Wang*, Liangbing Hu*

*Corresponding author. Email: binghu@umd.edu (L.H.); guw8@pitt.edu (G.W.); rsyassar@uic.edu (R.S.-Y.); chaowang@jhu.edu (C.W.)

Published 13 March 2020, *Sci. Adv.* **6**, eaaz0510 (2020)
DOI: 10.1126/sciadv.aaz0510

This PDF file includes:

Simulation details

Compositional pre-screening

To screen the possible structures for the MEA-NPs, two sets of rules, derived from well-studied high entropy alloy materials, were applied.[8,25,26,37]

(1) The solid solution phase (alloy) of the MEA, rather than the amorphous phase, forms when the composition weighted atomic radii difference δ is smaller than 6.5% and the mixing enthalpy ΔH_{mix} falls in the interval from -11.6 to 3.2 kJ/mol, where

$$\delta = \sqrt{\sum_i c_i \left(1 - \frac{r_i}{\bar{r}}\right)^2}$$

$$\Delta H_{\mathrm{mix}} = \sum_{i<j} 4\Delta H_{ij}\, \mathrm{c}_i \mathrm{c}_j$$

In this equation, c_i is the atomic ratio of the *i*th element, r_i is the atomic radius of the *i*th element, $\bar{r}$ is the averaged atomic radius, and H_{ij} is the enthalpy of mixing of the binary alloy calculated by Miedema's model.[38]

(2) To separate the solid solution phase from the intermetallic compound phase, the criterion could be expressed as

$$\Delta H_{mix} - T\Delta S_{mix} = \Delta G_{mix} < \Delta G_{IM} = \Delta H_{IM} - T\Delta S_{IM}$$

in which ΔS_{IM} is the entropy of formation of the MEA in the intermetallic (IM) phase and a linear relationship is assumed between the entropy, $\Delta S_{IM} = \kappa_2 \Delta S_{mix}$ where $\kappa_2 = 0.6$. ΔH_{IM} can be calculated from the enthalpy of formation values ΔH_{ij}^{IM} for binary intermetallic

$$\Delta H_{IM} = \sum_{i<j} 4\Delta H_{ij}^{IM}\, \mathrm{c}_i \mathrm{c}_j$$

Density functional theory calculations

We considered the following reaction describing the formation of the Ru-based MEAs from pure metals (the ratios are from actual compositions)

$$0.12\mathrm{Co_{hcp}} + 0.14\mathrm{Ni_{fcc}} + 0.44\mathrm{Ru_{hcp}} + 0.30\mathrm{Rh_{fcc}} \rightarrow 4 - \mathrm{HEA_{fcc}} \quad (1)$$

and

$$0.20\mathrm{Co_{hcp}} + 0.20\mathrm{Ni_{fcc}} + 0.25\mathrm{Ru_{hcp}} + 0.25\mathrm{Rh_{fcc}} + 0.10\mathrm{Ir_{fcc}} \rightarrow 5 - \mathrm{HEA_{fcc}} \quad (2)$$

The total energy difference between the reactants and products, i.e., the enthalpy of formation ΔH for reactions (1) and (2) were calculated to be 0.094 eV/atom and 0.079 eV/atom, respectively, suggesting that the MEA phase is energetically unfavorable at low temperature. The ideal configurational entropy change for MEA can be calculated using equation$\Delta S = -k_B \sum_i x_i \ln(x_i)$, where k_B is the Boltzmann constant and x_i is the chemical composition (molar ratio) of the *i*th element. Consequently, the equilibrium transformation temperature to form a single-phase solid solution MEA is calculated by $T_{\mathrm{trans}} = \Delta H/\Delta S$. For Ru-based 4-MEA and 5-MEA, the transformation temperature was predicted to be 871 K and 584 K, respectively. Following a similar computation scheme, we calculated the transformation temperature for the binary Ru-Ni disordered alloy to be 1930 K. Our DFT predictions demonstrate the role of entropy in the synthesis of MEAs. It should be noted that the DFT calculations were performed without taking the vibrational energy and surface energy effect of the NP into consideration. Also, the real configurational entropy in the NP should be lower than ideal configurational entropy due to short range ordering. As a result, the formation temperature predicted by our DFT is a lower limit.

Atomistic modeling by MD-MC

The MEA-NPs were modeled by NPs with a cuboctahedral shape and fcc crystal structure. The modeled NP contains 4033 atoms in total and has a size of ~5 nm. Initial structures were constructed by randomly assigning elements to each lattice site according to the nominal composition and followed by relaxation to release the local stress. Starting from these structures, Metropolis algorithm based Monte Carlo simulations was used to sample the possible atomic configurations. Within each MC iteration, a trail move that swaps the position of two atoms with different element type was performed. In each simulation, 2 million MC iterations were performed at 1500 K to evaluate the equilibrium atomic distribution of the NPs. A non-periodic boundary condition was assumed in all MC simulations. After the MC steps, the structures were

equilibrated at 298 K for 20 ns (20 million steps) through molecular dynamics (MD) simulations. To simulate the stability of the MEA NPs under different diffusion conditions, the NPs were further held at 773 K (and 298 K) for 10 ns in the MD simulation, during which MC trial steps swapping each pair of elements were attempted every *n* MD time steps, with *n* ranging from 2 ps (slow annealing) to 100 ps (rapid quenching). The equation of motion was integrated using the velocity Verlet algorithm with a time step of 1 fs.

Table S1. Predicted lattice constant *a* and enthalpy of formation ΔH for relevant binary and quaternary alloys using DFT and MEAM.

Alloy	Phase	*a* (Å)		ΔH(eV/atom)	
		DFT	MEAM	DFT	MEAM
Co_3Ni	$L1_2$	3.522	3.541	0.003	0.047
CoNi	$L1_0$	3.485	3.546	0.004	0.010
CoNi	B2	2.811	2.878	0.156	0.134
$CoNi_3$	$L1_2$	3.525	3.524	0.013	0.014
Co_3Rh	$L1_2$	3.633	3.594	0.050	0.050
CoRh	$L1_0$	2.656	2.591	0.073	0.073
CoRh	B2	2.975	2.975	0.162	0.161
$CoRh_3$	$L1_2$	3.790	3.719	0.044	0.044
Co_3Ru	$L1_2$	3.589	3.558	0.168	0.170
CoRu	$L1_0$	2.656	2.543	0.178	0.174
CoRu	B2	2.928	2.928	0.344	0.344
$CoRu_3$	$L1_2$	3.790	3.719	0.152	0.132
Co_3Ir	$L1_2$	3.634	3.612	0.046	0.046
CoIr	$L1_0$	3.689	3.671	0.037	0.036
CoIr	B2	2.961	2.961	0.253	0.253
$CoIr_3$	$L1_2$	3.794	3.737	0.047	0.048
Ni_3Rh	$L1_2$	3.627	3.563	0.030	0.030
NiRh	$L1_0$	2.661	2.538	0.046	0.054
NiRh	B2	2.940	2.940	0.133	0.133
$NiRh_3$	$L1_2$	3.787	3.692	0.041	0.041
Ni_3Ru	$L1_2$	3.626	3.556	0.150	0.150
NiRu	$L1_0$	2.598	2.509	0.158	0.158
NiRu	B2	2.922	2.922	0.270	0.270
$NiRu_3$	$L1_2$	3.755	3.691	0.188	0.187
Ni_3Ir	$L1_2$	3.631	3.601	0.045	0.030
NiIr	$L1_0$	3.702	3.662	0.039	0.049
NiIr	B2	2.942	2.942	0.139	0.134

$NiIr_3$	$L1_2$	3.814	3.731	0.085	0.039
Ru_3Rh	$L1_2$	3.821	3.802	0.080	0.100
RuRh	$L1_0$	2.694	2.671	0.059	0.086
RuRh	B2	3.073	3.071	0.510	0.334
$RuRh_3$	$L1_2$	3.834	3.800	0.036	0.048
Ru_3Ir	$L1_2$	3.831	3.811	0.025	0.026
RuIr	$L1_0$	3.832	3.823	-0.025	-0.014
RuIr	B2	3.094	3.094	0.593	0.249
$RuIr_3$	$L1_2$	3.860	3.833	-0.032	-0.025
Rh_3Ir	$L1_2$	3.849	3.813	-0.007	-0.007
RhIr	$L1_0$	3.845	3.826	-0.011	-0.011
RhIr	B2	3.092	3.092	0.449	0.299
$RhIr_3$	$L1_2$	3.867	3.835	-0.009	-0.008
CoNiRuRh	fcc	3.692	3.653	0.142	0.066
CoNiRuIr	fcc	3.697	3.650	0.112	0.066
CoNiRhIr	fcc	3.715	3.656	0.067	0.021
CoRuRhIr	fcc	3.765	3.722	0.083	0.099
NiRuRhIr	fcc	3.782	3.704	0.106	0.093

Table S2. ICP-MS result for our samples in the NH_3 decomposition experiment.

Composition	**Atomic Ratio**	**Loading wt% (on carbon)**
RuRhCoNi (Ru-4 MEA-NP)	$Co_{0.12}Ni_{0.14}Rh_{0.30}Ru_{0.43}$	25.6%
RuRhCoNiIr (Ru-5 MEA-NP)	$Co_{0.186}Ni_{0.172}Rh_{0.282}Ru_{0.273}Ir_{0.087}$	21.7%
RuRhCoNiIr (Ru-5 IMP, control)	$Co_{0.20}Ni_{0.20}Ru_{0.27}Rh_{0.28}Ir_{0.05}$	21.6%

Table S3. Simulated lattice distortion of the Ru-4 and Ru-5 MEA-NPs.

Distortion (Å)		Co	Ni	Ru	Rh	Ir
Ru-4	Min	0.0208	0.0180	0.0172	0.0118	
	Max	0.0574	0.0840	0.0795	0.0793	
	Mean	0.0356	0.0402	0.0440	0.0424	
Ru-5	Min	0.0306	0.0086	0.0179	0.0189	0.0170
	Max	0.1093	0.0735	0.0873	0.1043	0.0658
	Mean	0.0577	0.0468	0.0520	0.0545	0.0397

Table S4. Catalytic performance of NH_3 decomposition and comparison with the literature. (Figure 5e). (Reaction temperature 450°C)

Catalysts	Preparation	Ru (wt%)	GHSV (mL g_{cat}^{-1} h^{-1})	Conversion (%)	References
Ru/Al_2O_3	Impregnation	10%	30,000	31.5%	Appl. Catal. A-General 2004, 277, 1-9.
Ru/SiO_2	Impregnation	10%	30,000	34.5%	Catal. Lett. 2001, 72, 197-201.
Ru/TiO_2	Impregnation	4.8%	30,000	27.2%	Catal. Today 2004, 93, 27-38.
Ru/CNTs	Impregnation	4.8%	30,000	43.3%	Appl. Catal. A-General 2004, 277, 1-9.
Ru/MgO	Impregnation	4.8%	30,000	30.8%	Appl. Catal. B-Environ. 2017, 211, 167-175.
Ru/MgO-DP	Deposition-precipitation	3.5%	30,000	56.5%	Appl. Catal. B-Environ. 2017, 211, 167-175.
RuRhCoNi/C	Thermal shock	11%	36,000	75.0%	This work
RuRhCoNiIr/C	Thermal shock	5.9%	36,000	60.3%	This work
RuRhCoNiIr/C	Impregnation	5.8%	36,000	9.6%	This work (control)

Supplemental Figures

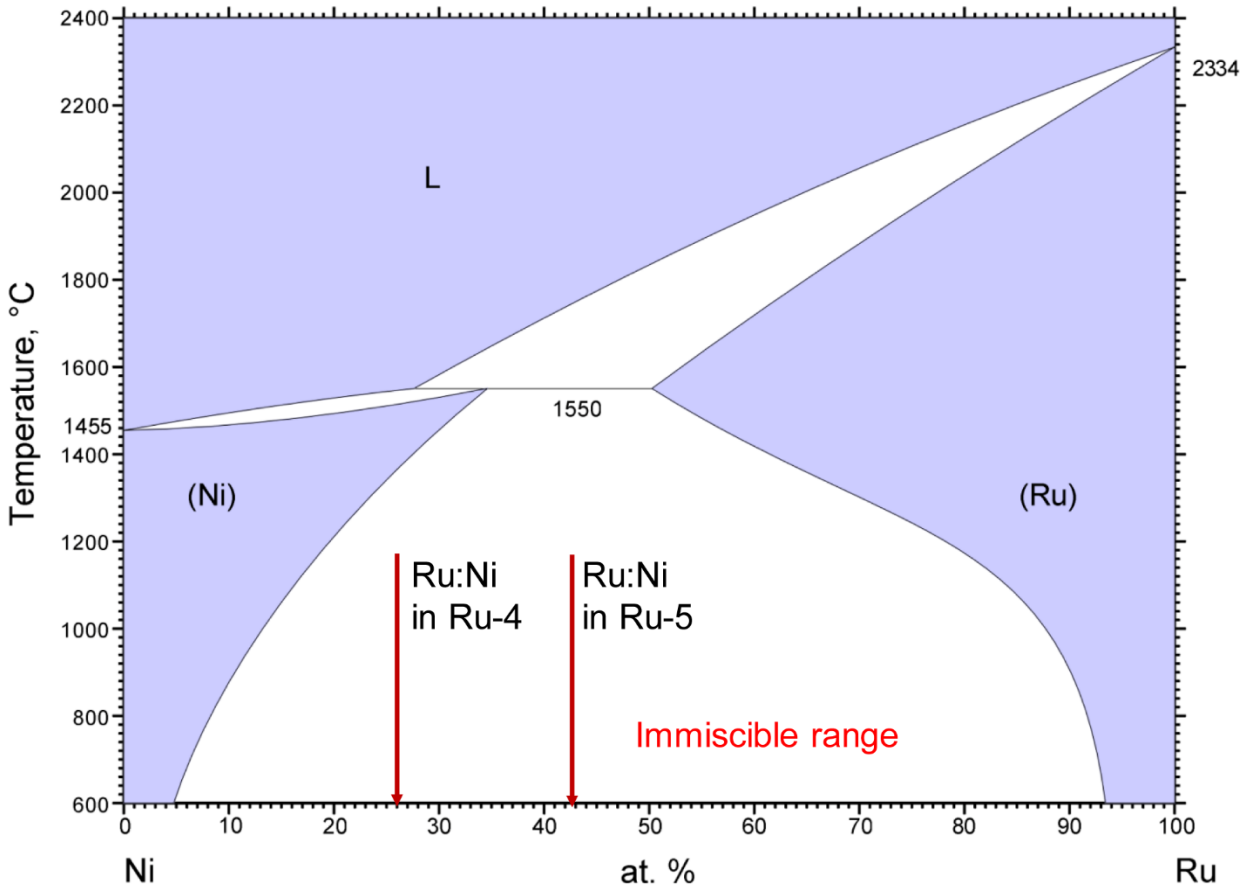

Fig. S1. Equilibrium phase diagram of Ru-Ni, showing a large immiscible gap. The Ru-4 and Ru-5 MEA-NPs synthesized in this study have Ru:Ni ratios in the immiscible range of the Ru-Ni bimetallic diagram. (Figure from ASM international)

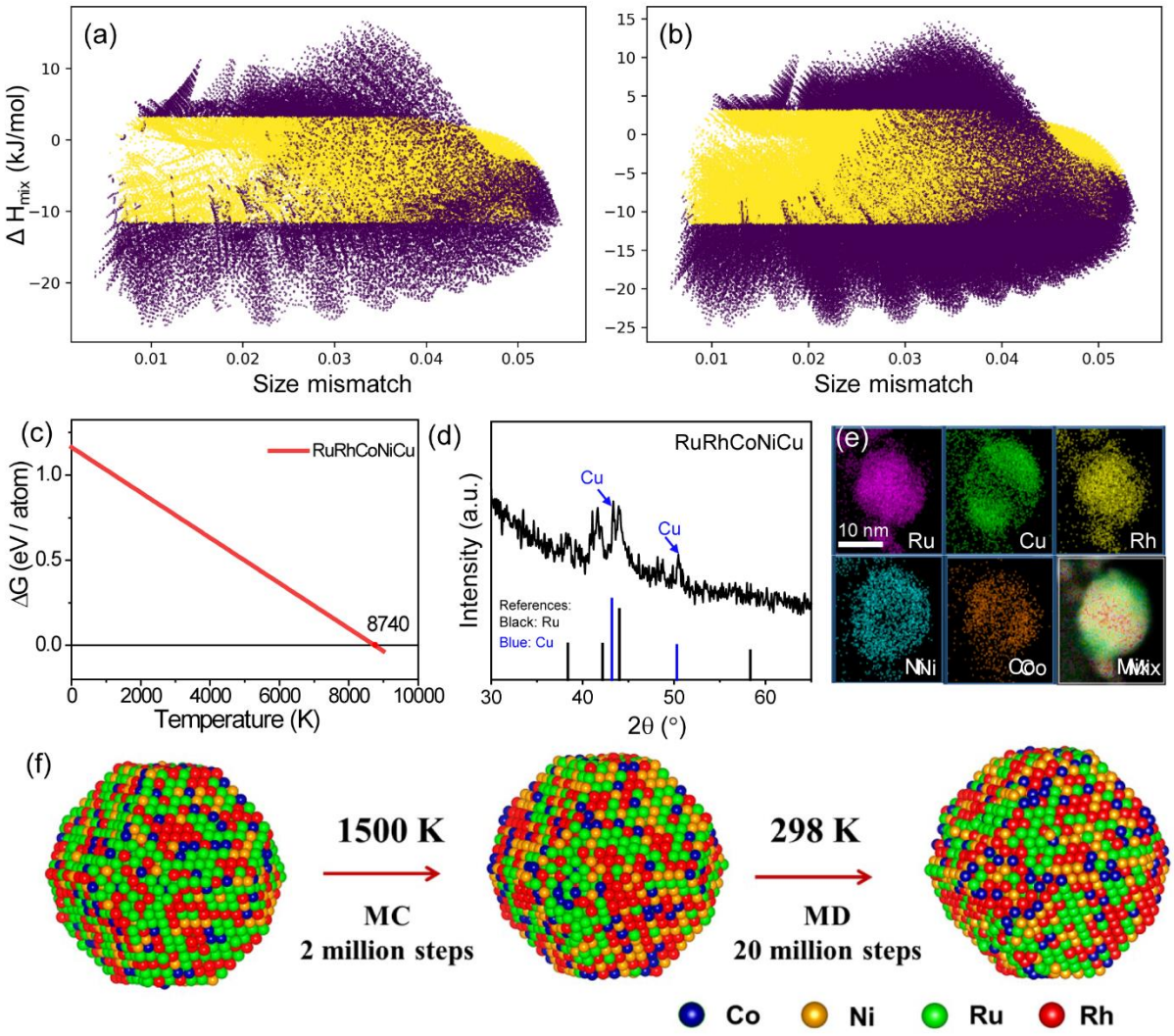

Fig. S2. MEA-NP composition screening and prediction. Phase selection diagrams for (a) quaternary and (b) quinary MEA-NPs made from the 10 catalytically active elements (Ru, Rh, Co, Ni, Ir, Pd, Cr, Fe, Cu, Mo) with compositions for each element from 5% to 50% with a step size of 5%. Non-alloy formation in $Ru_{0.25}Rh_{0.10}Co_{0.20}Ni_{0.15}Cu_{0.3}$ system. (c) DFT calculated temperature-dependent Gibbs free energy of a RuRhCoNiCu system, showing the thermodynamic alloy formation temperature of 8740 K. (d) XRD profile of RuRhCoNiCu with multiple peaks around 40-45º, indicating a mixture phase. (e) EDS maps of RuRhCoNiCu clear show a heterogeneous structure where Ru/Rh are immiscible with Cu. These results confirm the capability of our calculation to predict both alloy and non-alloy formation. (f) Hybrid MD-MC simulation of the formation and stabilization of Ru-4 MEA-NPs.

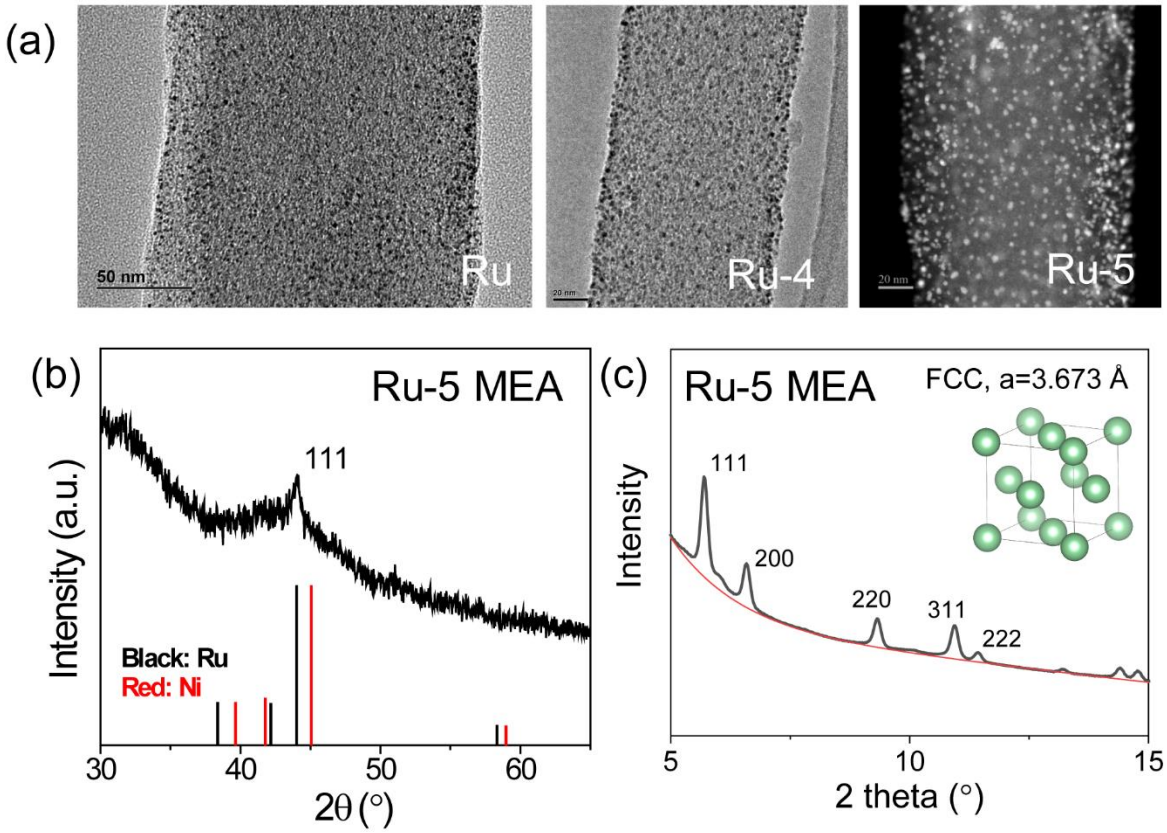

Fig. S3. Size distribution and macro structure of Ru-MEA NPs. (a) TEM and HAADF images of Ru, Ru-4 and Ru-5 MEA-NPs, which demonstrate ultra-small size and uniform distribution. (b) Powder XRD profile with a single peak, indicating single phase alloy structure for Ru-5 MEA-NPs. (c) Synchrotron XRD profile (λ= 0.2113 Å) of Ru-5 MEA-NPs, showing a clear single phase FCC structure with a fitted lattice constant of 3.673 Å, confirming the single phase alloy formation.

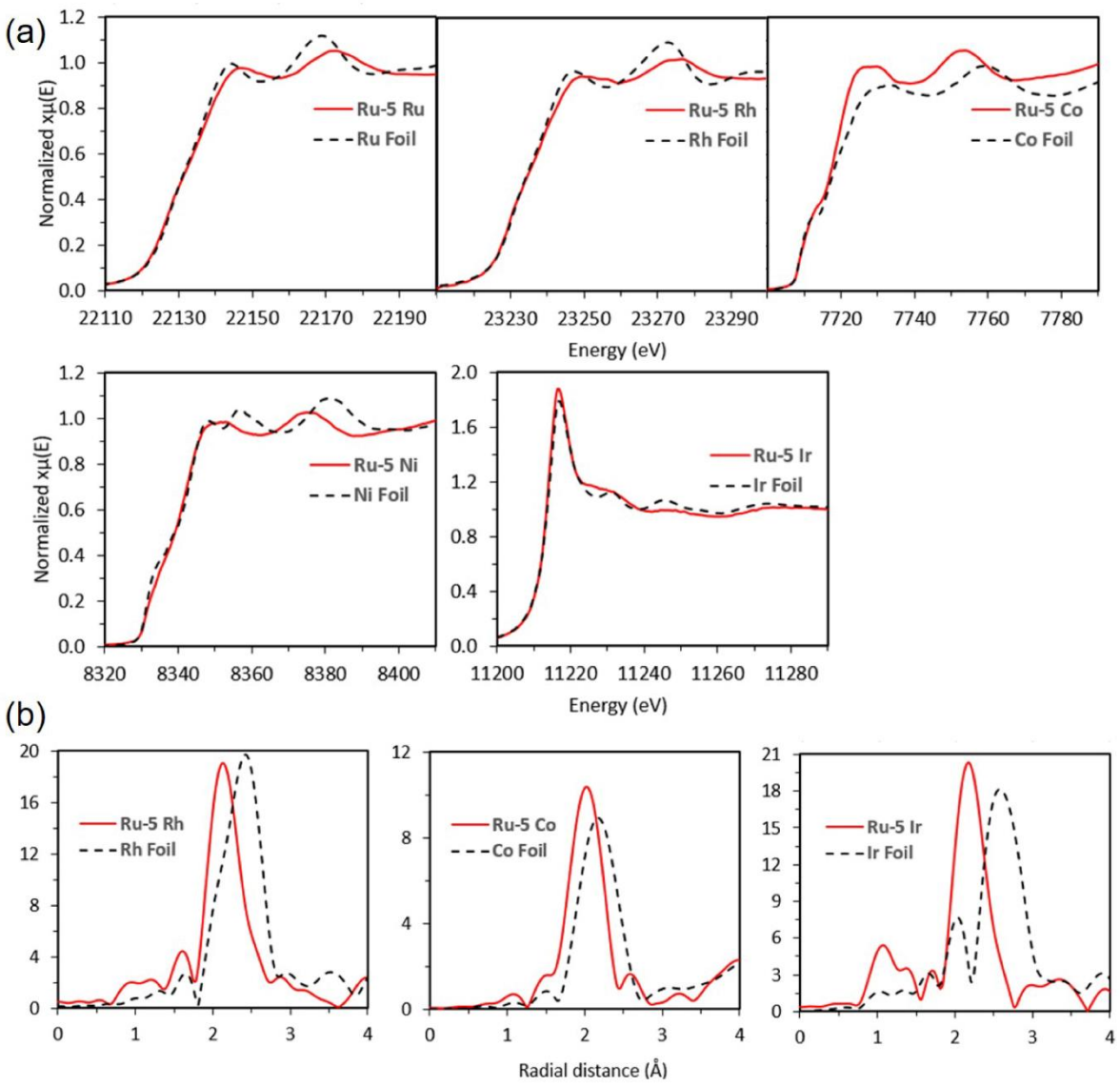

Fig. S4. X-ray absorption spectra for Ru-5 MEA-NPs. (a) The XANES spectra of each element in Ru-5 MEA-NPs, indicating these elements are in the metallic state due to the similarity in their absorption edge profile with the corresponding metallic references. (b) The FT-EXAFS profiles of Rh, Co, Ir elements in Ru-5 MEA-NPs compared with their corresponding metal foils. The slight shift indicates these elements are not in a pure unary metallic state but surrounded by different elements, i.e., an alloy state.

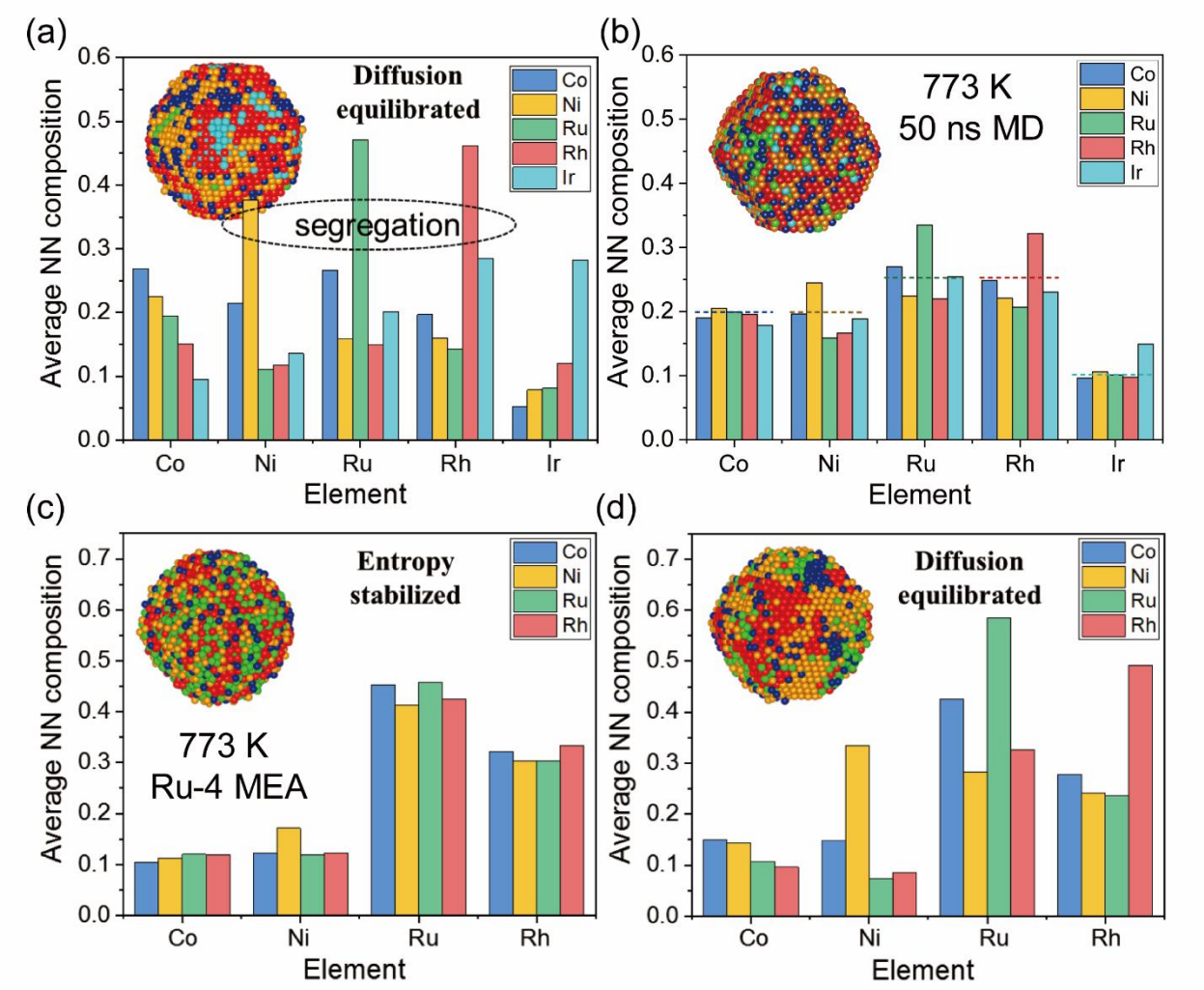

Fig. S5. Hybrid MC + MD simulation on MEA-NP stability after annealing. (a) Nearest neighbor compositional analysis of fully equilibrated Ru-5 MEA-NPs at 773 K, which shows segregation for Ru, Rh, and Ni. (b) Simulation of kinetic stability of Ru-5 MEA-NPs at 773 K using 50 ns timescale MD. (c)-(d) Nearest neighbor compositional analysis of entropy-stabilized Ru-4 MEA-NPs versus a diffusion equilibrated structure using a coupled MD-MC simulation at 773 K.

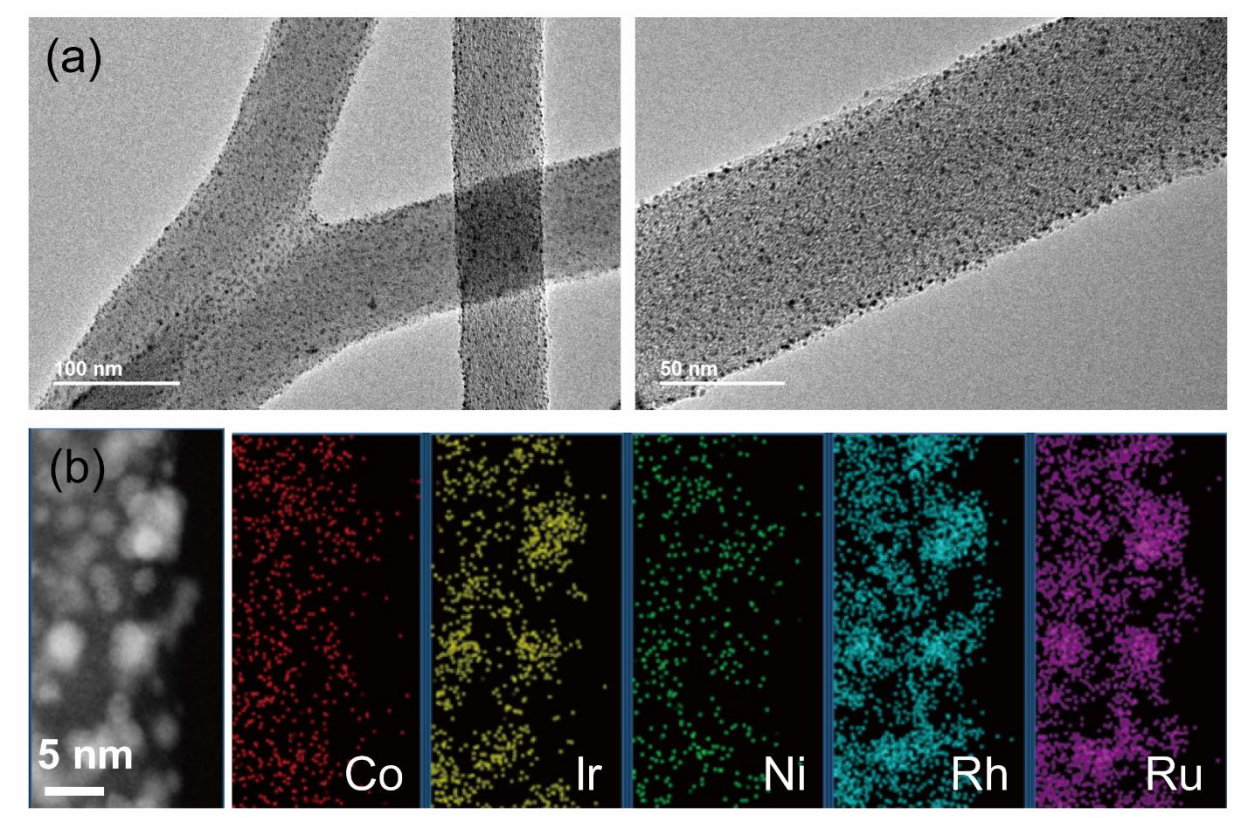

Fig. S6. Ru-5 control samples prepared by impregnation method. (a) TEM images of the Ru-5 IMP NPs. (b) HAADF image and corresponding mapping of the Ru-5 IMP NPs. The brighter particles are noble metals (Ru, Rh, Ir) and the gray particles are non-noble metals (Co, Ni).